

A Study of Fan-Distortion Interaction Within the NASA Rotor 67 Transonic Stage

V. Jerez Fidalgo¹

C. A. Hall

Y. Colin

Whittle Laboratory,
University of Cambridge,
1 JJ Thomson Avenue,
Cambridge CB3 0DY, United Kingdom

The performance of a transonic fan operating within nonuniform inlet flow remains a key concern for the design and operability of a turbofan engine. This paper applies computational methods to improve the understanding of the interaction between a transonic fan and an inlet total pressure distortion. The test case studied is the NASA rotor 67 stage operating with a total pressure distortion covering a 120-deg sector of the inlet flow field. Full-annulus, unsteady, three-dimensional CFD has been used to simulate the test rig installation and the full fan assembly operating with inlet distortion. Novel post-processing methods have been applied to extract the fan performance and features of the interaction between the fan and the nonuniform inflow. The results of the unsteady computations agree well with the measurement data. The local operating condition of the fan at different positions around the annulus has been tracked and analyzed, and this is shown to be highly dependent on the swirl and mass flow redistribution that the rotor induces ahead of it due to the incoming distortion. The upstream flow effects lead to a variation in work input that determines the distortion pattern seen downstream of the fan stage. In addition, the unsteady computations also reveal more complex flow features downstream of the fan stage, which arise due to the three dimensionality of the flow and unsteadiness. [DOI: 10.1115/1.4003850]

Introduction

Distortion issues are present in both civil and military aero engine compression systems. They are often non-negligible and the stability of the whole engine can be put at risk if their potential for consuming the available surge margin is underestimated. Furthermore, with the perspective of novel civil aircraft architectures in mind as well as the increasingly complex military propulsion systems, it appears that the idea of efficient and robust gas turbine engines capable of operating continuously with distorted inlet conditions will soon become a reality. The first step in this direction must be given in terms of understanding better the underlying physics of such flows. In this sense, high fidelity CFD capabilities must be exploited. From this perspective, investigating distorted flows in turbomachines adds a number of difficulties. First, assuming flow axisymmetry or periodicity over one pitch is no longer possible, which means that the whole of the annulus must be considered. Furthermore, the combination of the incoming flow's asymmetry with rotating blade rows calls for a time-accurate solution procedure. Not only does this mean that obtaining reliable solutions can be very costly, but also extracting meaningful and concrete information from them is challenging.

Conceptually, significant progress was done on distortion transfer understanding up to the 1970s thanks to the development of inviscid and incompressible analytical methods based on linearized versions of the equations of motion and conservation of vorticity. A considerable number of publications [1–10] provide very illustrative (although simplified) descriptions of the interaction between turbomachinery blade rows and distortion. In the 1980s Hynes and Greitzer [11] came up with a formulation to account for unsteady effects within the passages of rotors subject to circumferentially varying inlet conditions that became quite popular. Their model, based on Moore's [12], estimated that the static pressure differences over and above that indicated by the quasi-steady pressure rise rotor characteristic should be proportional to the

airfoil chord length and the angular rate of change of inlet axial velocity. Its main limitation was related to the assumptions made: two-dimensional, incompressible flow.

The importance of component coupling in distorted flows is identified in [5–7]. These studies demonstrated that a compressor would induce an irrotational velocity field ahead of it in response to the incoming distortion. This inviscid interaction would in turn have a strong impact on the rotor's lift as the relative incidence angle and velocities have a first-order dependence on the circumferential velocity component at the fan face. Additionally, such induced velocity field associated to the upstream distortion attenuation is related to the rotor's bound and shed vorticity. Further studies by Greitzer [13] based on Mazzawy's [14] showed that there might also exist a strong coupling between the rotor flow field and the downstream components when a compressor is subject to inlet distortion. Indeed, Longley and Greitzer [15] pointed out that the length scale of flows with circumferential distortion is the mean radius, and this can be large compared to the distance between components. Hence, in the presence of distortion, components can interact much more strongly than in clean flow. In this sense, the circumferential extension of the distortion pattern is also of great importance. Longley and Greitzer [15] also highlighted the fact that the different spatial harmonics of circumferential distortion experience different degrees of coupling because the ratio of axial distance between components and the wavelength of the harmonic will differ. It is the low spatial harmonics that show the strongest effects and hence the emphasis of research on large extent distortions.

There are several methods available nowadays to analyze distortion effects. Apart from URANS, which have only recently become available in this context, these are namely parallel compressors [14], actuator disks [16–18], and time-accurate Euler methods with body forces [19,20] included as source terms to account for viscous effects and/or blade forces. Nevertheless, as of today, no method (apart from URANS) has proved to be able to simulate accurately the interaction between transonic turbomachines and incoming distortion.

Only recently have URANS methods been applied to whole-annulus distortion flows in fans and compressors, mainly because of their computational cost. An interesting example by Hah et al. [21] illustrates how much more complicated the unsteady flow

¹Corresponding author, e-mail: vj229@cam.ac.uk

Contributed by the International Gas Turbine Institute (IGTI) of ASME for publication in the JOURNAL OF TURBOMACHINERY. Manuscript received January 14, 2011; final manuscript received January 29, 2011; published online May 8, 2012. Editor: David Wisler.

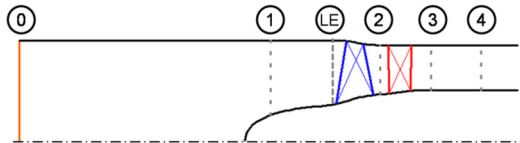


Fig. 1 NASA R67 fan-stage meridional view with distortion screen position (station 0), measurement planes (stations 1, 2, 3, and 4), and leading edge station (LE)

within the passages of a rotor operating with inlet distortion can be when compared to its steady, clean flow counterpart. More recently, Yao, Gorrell, and Wadia [22–25] have presented results obtained after running full-annulus, unsteady CFD on two half multistage military-type fans for which experimental data was available. Within these, an explanation is made of how the local operating condition of each stage is estimated to vary circumferentially. The issue of the existence of an angular shift between stagnation pressure and temperature downstream of a rotor operating with distortion is also raised.

This paper sets out to: (i) demonstrate accurate simulation of a representative test case using high fidelity CFD, (ii) explain properly how the fan is operating at different locations around the annulus, and (iii) show how the exit flow field is mainly determined from the fan operating condition and the variations in the inlet flow field.

To achieve these aims, a single-stage, transonic fan for which previously unpublished distortion experimental data is available has been used. The distortion pattern is purely circumferential with two distinct regions of inlet flow: clean and distorted. This makes it easier to follow how the flow develops through the fan stage. Following the description of the numerical approach, the redistribution of the approaching flow upstream of the fan is presented and examined. A new method is used to derive the overall performance of the fan and its effective variation around the annulus from a quantitative point of view and to the authors' knowledge, this is the first time that such results are presented. The development of the flow through the rotor is then presented and explained in terms of the upstream swirl and mass flow redistribution. Finally, experimental measurements downstream of the rotor and the stage are compared with the CFD results, demonstrating that the CFD accurately captures the distortion transfer.

The Test Case

The test case chosen was the NASA rotor 67 transonic fan stage (Fig. 1).

The version tested with inlet distortion features a rotating full spinner configuration and consists of a first rotor row with 22 multiple-circular-arc blades and a stator row (S67A) with 34 controlled-diffusion airfoils (Fig. 2), resulting in a blade count ratio slightly above 1.5.

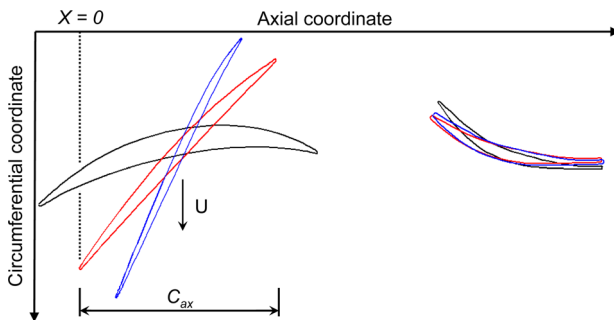


Fig. 2 Representative rotor and stator blade sections at three spanwise locations: hub (black), midheight (blue), and casing (blue)

When operating at 100% speed, the stage total pressure ratio is close to 1.6 and the corrected mass flow is 33.25 kg/s, resulting in a rotor tip inlet relative Mach number of 1.4. Other key rotor parameters are presented in Table 1. A complete description of the rig and details of the aerodynamics of the stage operating without the spinner and with different stator geometries in clean flow is provided in Refs. [26–31].

The tests were carried out at the W8 Single Stage Compressor Test Facility [32] at NASA Glenn Research Centre, Cleveland, Ohio, USA. The distortion pattern consisted of a 120 deg low-total-pressure region generated with a distortion screen located far upstream. Tests were carried out for a number of different rotational speeds ranging from 70% to 100%. The instrumentation available at each measurement station consisted of static pressure tappings at both hub and casing, "cobra" probes to measure radial profiles of total pressure, temperature and flow angle, and "wedge" probes to measure radial profiles of static pressure. In addition, total pressure and temperature rakes were positioned further downstream of the stage. The instrumentation was located at fixed circumferential positions. However, for some operating conditions, the distortion screen was sequentially rotated by increments of 30 deg to generate complete circumferential traverse data.

The operating speed selected for the distortion study in this paper was 90% of the design speed since severe stator separations were expected when operating with distortion at higher speeds. The particular operating condition chosen, for which extensive measurement data was available, corresponded to a corrected mass flow of 32 kg/s based on inlet, mass-averaged, stagnation quantities and a DC_{120} of 83%.

Computational Approach

The CFD solver employed in this work was Rolls-Royce's HYDRA [33]. HYDRA solves the unsteady, compressible, Reynolds-averaged, Navier-Stokes (RANS) equations on unstructured grids using a finite volume approach. The spatial discretization of the mean flow equations is based on an upwind Roe scheme. To provide for efficient, time-accurate solution of the RANS equations, an explicit dual time-stepping (DTS) procedure with a second-order backward differencing is employed. A four-stage Runge-Kutta scheme is used for the inner loop to achieve the convergence of the subiterations. The scheme is employed with multigrid techniques coupled to a Block-Jacobi preconditioner, improving its damping properties for highly stretched meshes inherent to RANS computations. HYDRA has been extensively used for turbomachinery applications and its continuous development over the years has extended its versatility to a number of aero-engine design applications. The analysis presented here used the Spalart-Allmaras, one-equation turbulence model [34] for resolving the eddy viscosity.

The computational domain is shown in Fig. 3. This reproduced, with a high level of accuracy, the complete experimental rig and installation. It consisted of four zones separated by sliding planes: the upstream duct, the rotor, the stator row, and the downstream choked nozzle.

Experimental values of absolute total pressure and temperature, null flow angles, and a standard value for the turbulence intensity

Table 1 Rotor alone main characteristic parameters at 100% speed

N (rpm)	16043
FPR	1.63
η_{is} (%)	92
Tip M_{rel}	1.38
Midspan Φ	0.65
Midspan ψ	0.5
AR	1.56
Mean r_h/r_t	0.43
D (m)	0.51

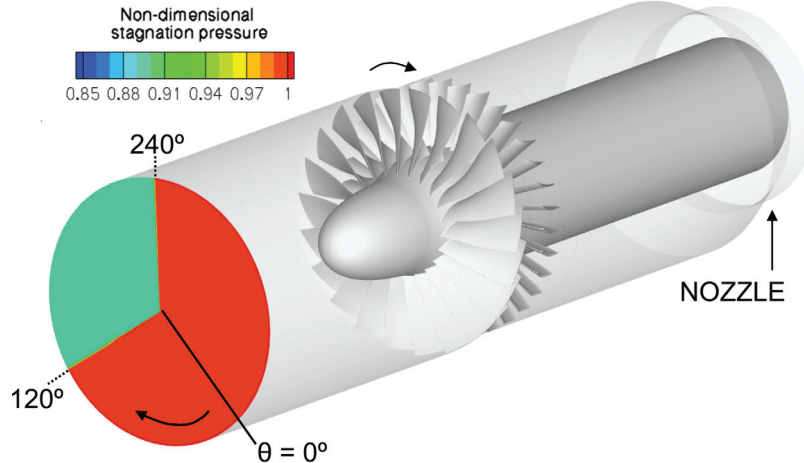


Fig. 3 Isometric view of the computational domain

were used to build the inlet boundary conditions. These were imposed far upstream, right where the distortion screen was located in the rig. Figure 4 shows a comparison of the total pressure measured at station 1 compared with computational results. This demonstrates that the distortion imposed in the CFD was consistent with the experiment. It also indicates that some mixing occurs between the clean and distorted sectors within the upstream duct. In the CFD, the inlet total pressure profile was assumed to follow a perfect square wave, and total temperature was assumed to be uniform.

A choked nozzle with additional bleeds was placed downstream of the stage to impose the exit boundary condition (Fig. 3). In this way, the correct mass flow can be indirectly specified instead of an unknown static pressure field. The accelerating part of the nozzle must be located sufficiently far downstream of the stage exit. It is important to prevent any coupling from happening by avoiding any static pressure distortion generated by the nozzle due to the incoming distortion interacting with the fan OGVs. The use of such exit boundary conditions have been shown to contribute to the enhancement of calculation stability near compressor stall conditions [35].

The meshing strategy for the stage was developed to limit the computational resources required for the unsteady calculations. Given that the objective of the study was to investigate bulk distortion interaction and transfer, the smaller-scale structures such as corner separations and tip-leakage vortices were not required to be resolved with a high level of detail. Overall, the grids were

kept relatively coarse (see Fig. 5 and Table 2). The grid generator used is Rolls-Royce's PADRAM [36].

Every effort was made to reach a satisfactory balance between mesh quality and size. All the rig geometrical details, such as the rotor's 1.78-mm-radius hub fillet, were included in the grids. The sensitivity of the calculations to the mesh density was explored through steady and unsteady computations using a range of grid sizes. It was found that the unsteady computations are more demanding in terms of the number of grid radial planes required to achieve grid insensitivity. The size of the smallest elements in the O-meshes around the blade surfaces were also limited in order to speed up the convergence of the inner loop of the computations. The resulting Y^+ values on the blade surfaces as well as on hub and casing walls were kept sufficiently low.

The final total grid size was approximately 42.5×10^6 elements, resulting in wall-clock running times that ranged between one and two months on a 128 CPUs cluster when starting from an initial solution obtained from a mixing plane, clean flow calculation. Convergence was typically obtained after 20–30 rotor revolutions

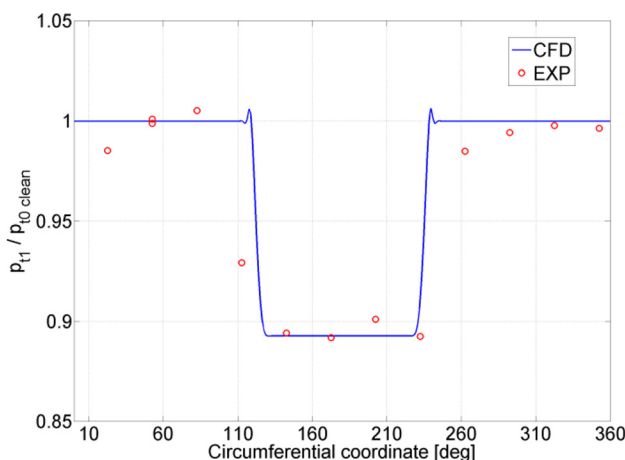


Fig. 4 Time-averaged, total pressure circumferential traverses at midspan, at measurement station 1

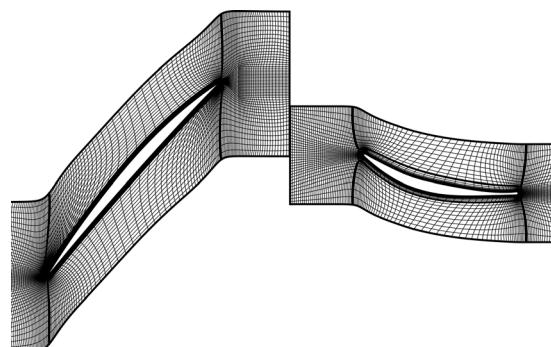


Fig. 5 Rotor and stator grids at midspan

Table 2 Distribution of grid elements among the different zones

	Domains/zone	Size/domain	Size/zone
DUCT	1	3.14×10^6	3.14×10^6
ROTOR	22	1.18×10^6	25.96×10^6
OGV	34	0.33×10^6	11.08×10^6
NOZZLE	1	2.27×10^6	2.27×10^6
TOTAL			42.46×10^6

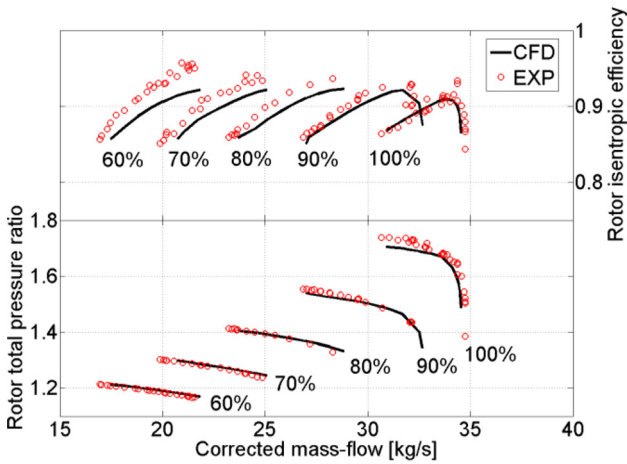


Fig. 6 Clean flow total pressure ratio and efficiency characteristics for rotor alone configuration

were completed. The number of physical time steps per period varied throughout the calculation, with a maximum of 2200 time steps for the last revolutions. Table 2 shows how the cells were distributed among the four different zones.

Overall Performance in Clean Flow

Figure 6 shows the total pressure ratio and isentropic efficiency characteristic maps for the rotor alone operating with uniform, clean inflow.

The numerical characteristics were computed using steady, rotor-alone calculations on exactly the same grids as those applied in the full-annulus unsteady computations. The agreement between CFD and experimental data is very encouraging. There is a close match in the shape of all the characteristic curves and the absolute levels of pressure ratio and choking mass flow agree well. At part speeds, the predicted efficiency values are lower than the measured values, although the measured trend in increasing efficiency at low speed is unexpected.

Fan Upstream Influence in Distorted Flow

When subjected to inlet total pressure distortion, the fan stage faces an incoming flow field with a mass-flow distribution that varies around the annulus. The rotor reacts to this mass-flow asymmetry in a way that tends to suppress it: the regions of low mass flux push the fan local operating point towards higher pressure ratio and as a result, the static pressure upstream of the fan is

reduced. In other words, the fan rotor sucks harder on the regions with lower total pressure (and lower mass flux). This effect is clearly visible in Fig. 7, which shows the circumferential distribution of static pressure and mass flux at three axial locations upstream of the fan rotor. As the rotor is approached, the static pressure in the distorted region falls and this forces the mass flux distribution to become more uniform.

The nonuniform static pressure field upstream of the rotor generates flow in the circumferential direction. At a given axial position, flow from the undistorted regions is driven towards the distorted sector, where the static pressure is lower. This results in swirl being induced upstream of the rotor and as the rotor is approached the magnitude of these swirl variations intensify. Figure 8 shows the distribution of swirl angle at three axial locations upstream of the rotor and also shows measured results at measurement station 1. As the rotor enters the distorted sector (around 120 deg) it is within a region of co-swirl, which will tend to reduce the incidence onto the blades. As the rotor leaves the distorted sector (around 240 deg) it is within a region of counter-swirl, which will increase the incidence onto the blades. These incidence variations, in combination with the mass flow distribution, determine the amount of work that is locally put into the flow by the rotor. The impact of the nonuniform work input on the distortion transfer is explored further in later sections.

Radial flow is also induced by the upstream static pressure field from the rotor, affecting further the spanwise distributions of fluid properties. However, in the particular case of this fan stage, there is a more significant source of nonuniformity within the upstream flow field. It affects the rotor's hub region and it originates as a

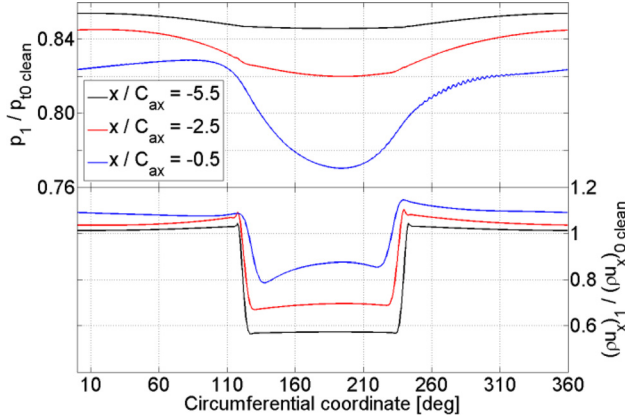


Fig. 7 Time-averaged, circumferential distributions of static pressure (top) and mass flux (bottom) for three axial locations ahead of the rotor

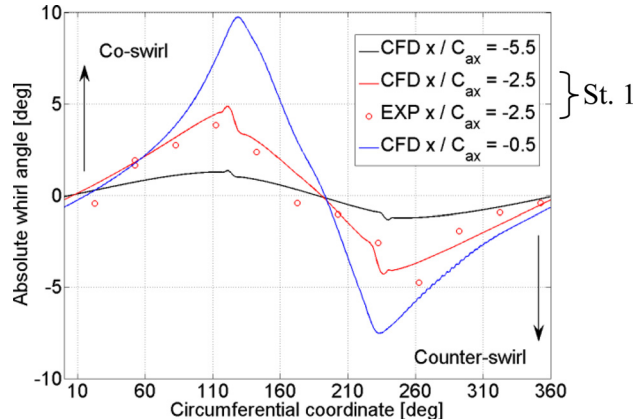


Fig. 8 Time-averaged, circumferential distributions of absolute whirl angle ahead of the stage at midspan

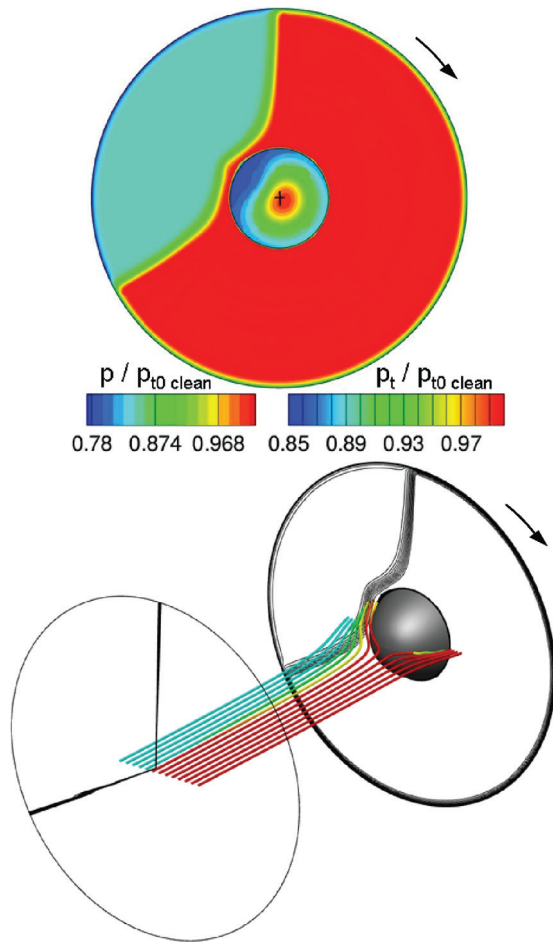


Fig. 9 Time-averaged flow in the upstream duct. Contours of stagnation pressure stations 0 and 1, contours of static pressure on spinner, and duct streamlines

result of the interaction between the incoming distortion and the rotating spinner. In clean inflow conditions, the center of the spinner nose would be a stagnation point. In the presence of distortion, however, the location of this stagnation point changes because as the flow is slowed down, the clean flow approaching the spinner

has a higher static pressure than that of the approaching distorted flow. This imbalance results in a displacement of the stagnation point towards the clean flow region (see Fig. 9). Consequently, some clean fluid migrates towards the distorted sector close to the hub. This is clearly shown by the streamlines within Fig. 9, and the stagnation pressure contours at station 1, which indicate that the flow at the hub originates in the clean flow.

There is also evidence of the above interaction with the spinner within the experimental data. In Fig. 10 total pressure profiles are shown at two circumferential positions around the annulus. Within the distorted region, close to the hub, the total pressure measured exceeds the far upstream value. Given that the flow close to the hub will also be affected by the spinner boundary layer, then this higher total pressure is most likely to be the result of flow coming from the clean sector. Additionally, since the local flow incidence onto the spinner is not zero, a nonaxisymmetric static pressure field is generated around the hub of the fan (see Fig. 9). The part within the distorted flow region forms a suction surface and the surrounding fluid is driven towards this area. Hence, swirl and local radial velocities are generated (see Fig. 11). These are in addition to the velocities generated by the more global upstream interaction between the rotor and the distortion. Figure 11 clearly shows the formation of a “jet” (high p_t) of fluid with high radial angle very close to the hub as a consequence of the incidence onto the spinner. This feature can be tracked all the way through the stage, as shown later.

Performance in Distorted Flow

The overall performance of the rotor operating with distortion is summarized in Table 3. This compares the time-averaged and mass-averaged performance parameters from the full annulus calculation with those obtained from single-passage computations with clean inflow.

Also of particular interest is how the performance varies around the annulus as the rotor travels in and out of the distortion. In order to be able to investigate this, a time-averaged solution evaluated in the frame of reference to which distortion is associated (the absolute one) is required. This is not straightforward to calculate for a rotating row, since each of the rotor blades is located at a different angular position at each time step and therefore the method used must carefully eliminate the blades from the final time-averaged solution. The procedure followed was based on gate functions, as described by Adamczyk [37]. This methodology reduces the computational requirements for post-processing to a level that is more manageable. Once the absolute-frame, time-averaged flow field has been determined, standard streamlining

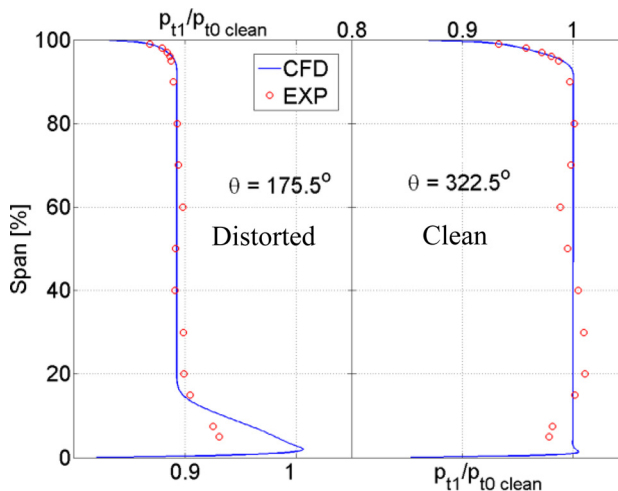


Fig. 10 Time-averaged radial traverses of stagnation pressure at station 1 in the distorted (left) and clean (right) sectors of the inlet flow field

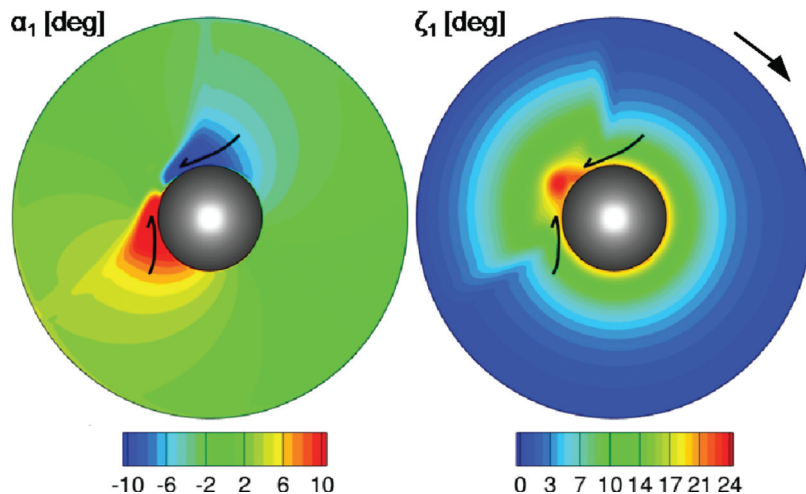


Fig. 11 Contours of time-averaged absolute whirl and radial angles at station 1

Table 3 Overall mass-averaged performance with and without distortion for the operating point of interest

	CFD (distortion)	CFD (clean)
Speed (%)	90.0	90.0
FPR (rotor)	1.46	1.46
m_{corr} (kg/s)	32.0	32.0
η (%)	92.0	93.5

procedures can be used to compute time-averaged particle paths. This streamlining capability can then be used for a number of post-processing purposes. For instance, in this study, it was used to divide the annulus, at a specified axial location upstream of the rotor, into identical sectors and the development of initially radial stream surfaces was tracked through the rotor domain.

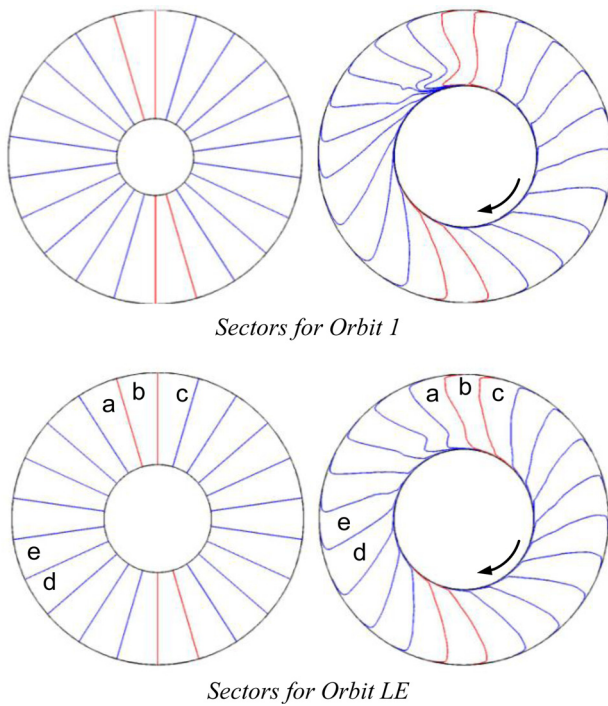


Fig. 12 Inlet (right) and exit (left) sectors used for calculating the rotor local operating condition: the “orbit” around the mean point

This enabled the entire rotor flow field to be divided into continuous stream tubes within the time-averaged flow field (see Fig. 12). This makes it possible to accurately compute sector-averaged pressure ratios and efficiency across the rotor. The accuracy of this approach was checked by confirming that the mass flows at inlet and exit from each sector stream tube were identical. The procedure was applied twice; for two different inlet planes. In the first case, the upstream plane chosen was measurement station 1 and the downstream plane was set just downstream of the rotor TE (orbit 1). In the second case, the procedure was repeated using an upstream plane that was located just upstream of the rotor’s LE (orbit LE). The aim was to calculate the locus of operating points followed by the fan rotor on the pressure ratio – mass flow characteristic. This locus of operating points is colloquially called an “orbit” and two different inlet locations were chosen in order to explore how the orbit was influenced by the upstream flow redistribution described in the previous sections. The resulting orbits of total pressure ratio against corrected mass flow are shown in Fig. 13. This also shows the steady characteristics for the rotor plus three additional results. The first (CLEAN CFD) represents the mean operating condition of a full-annulus, unsteady calculation with uniform inflow. This case was run in order to establish a true back-to-back comparison between clean and distorted flow calculations by making sure that there were no major time-averaged effects on the mean values due to the unsteadiness associated to rotor-stator interaction (these would not be captured by mixing-plane calculations). The second

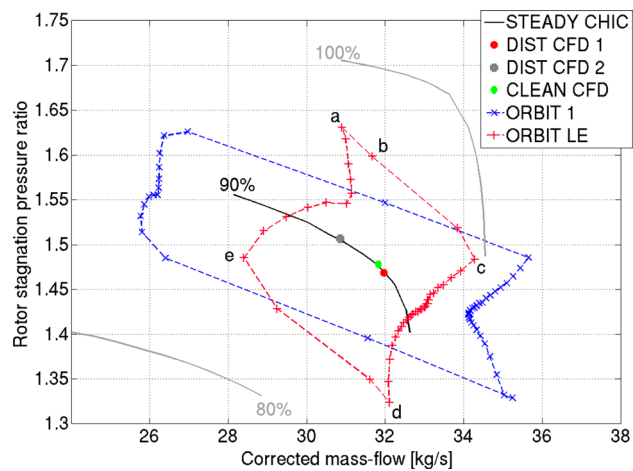


Fig. 13 The variation in local rotor operating conditions when operating in distortion

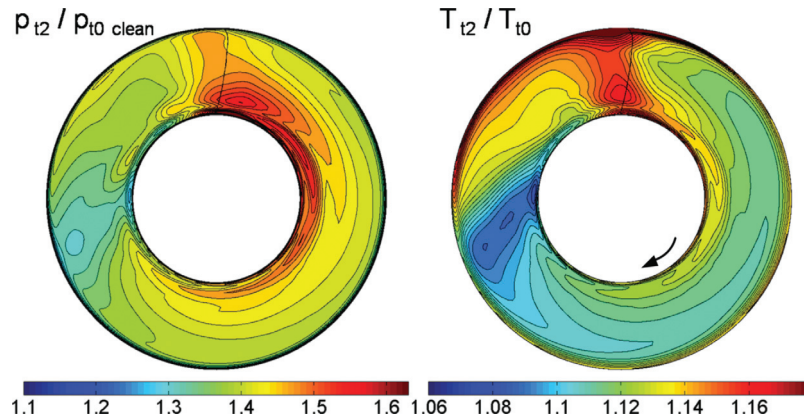


Fig. 14 Time-averaged total pressure (left) and temperature (right) at station 2

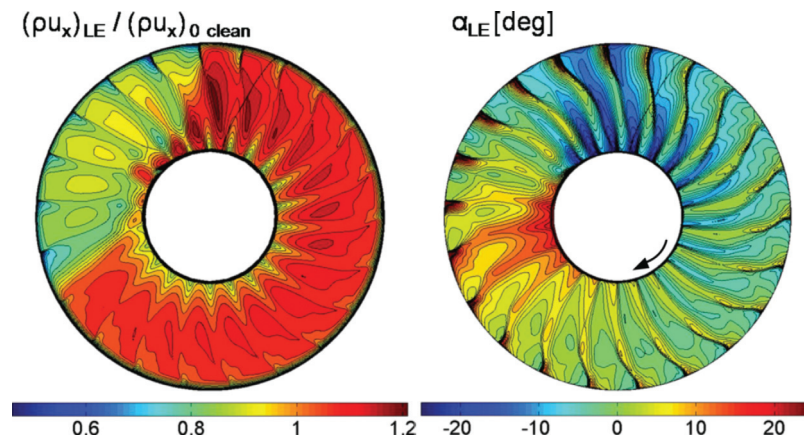


Fig. 15 Snapshots of mass flux and absolute whirl angle at rotor's LE

(DIST CFD 1) represents the mean operating condition of the full-annulus distortion calculation presented in this paper case (for which the two sets of orbits were calculated). It is quite interesting to notice that despite the strong variation of local operating condition around the annulus, the mean total pressure ratio falls right on top of the steady characteristic. The same is not true for the isentropic efficiency, whose mean value is slightly lower than the corresponding steady value (for simplicity, maps of efficiency and corresponding orbits are not shown here). There is a third result (DIST CFD 2) representative of the mean operating condition of a second distortion calculation ran with the same distortion pattern but at a lower mass flow. Once again, the mean total pressure ratio falls right on top of the steady characteristic.

Orbit 1 indicates how the local operating point of the rotor, based on inlet conditions at measurement station 1, is subject to large excursions in operating point, both in terms of mass flow and pressure ratio. The corrected mass flow varies by almost 30%, which initially appears excessive. However, as shown in Fig. 7, the variation in mass flux at measurement station 1 is indeed around 30%. The variations in pressure ratio around the annulus indicate the variation of work input provided by the fan rotor as the upstream inlet swirl and the mass flow nonuniformity lead to changes in the inlet velocity triangles. This is discussed further below. The differences between the two orbits in Fig. 13 arise as a result of the flow redistribution that takes place ahead of the fan stage. As the rotor is approached, the circumferential nonuniformity in mass flow is

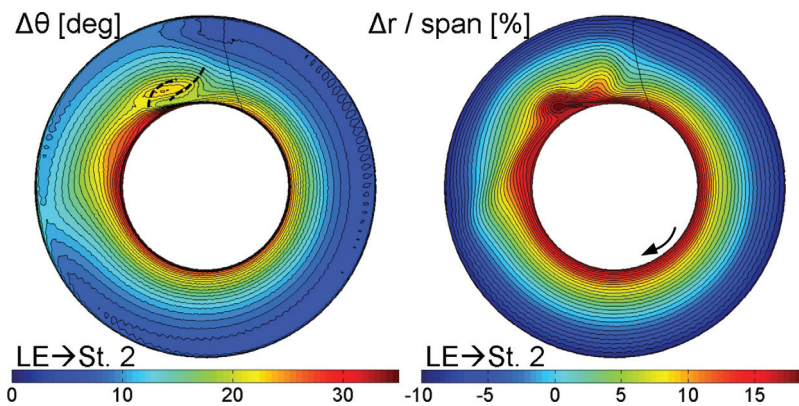


Fig. 16 Time-averaged particle displacements between the rotor's LE and TE: circumferential and radial

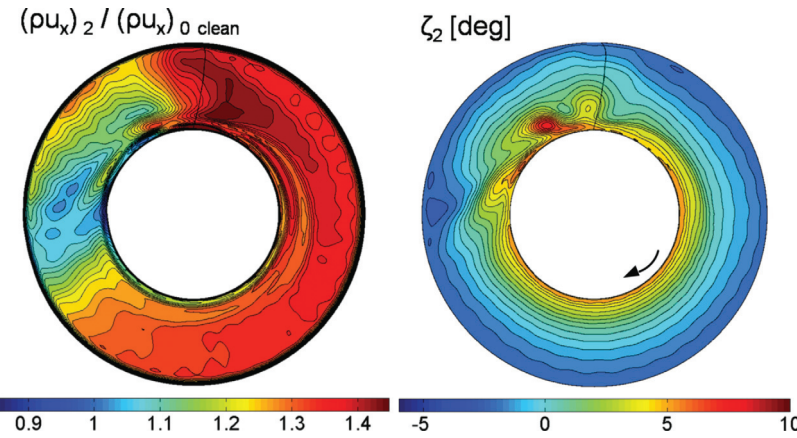


Fig. 17 Time-averaged mass flux and radial angle at station 2

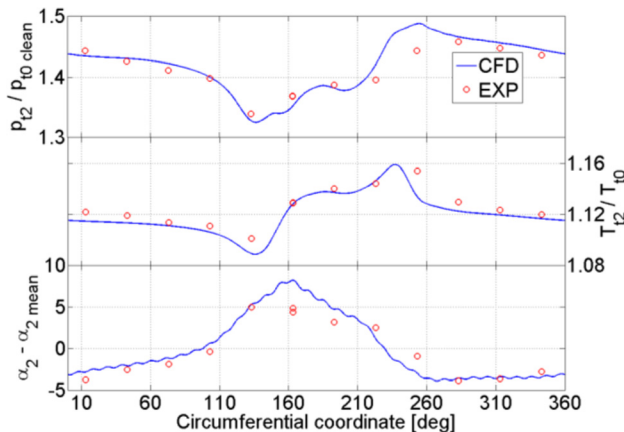


Fig. 18 Time-averaged circumferential traverses downstream of the rotor at midspan

reduced, as shown in Fig. 7. Thus, the excursions in mass flow are similarly reduced in the orbit based on inlet conditions just upstream of the rotor LE (orbit LE). Similarly, as the swirl nonuniformity is intensified, the changes in fan pressure ratio are increased. It is worth noting that many of the local operating points described by orbit 1 are beyond the stability boundary of the clean flow characteristics. However, all the points within orbit LE are

within the stability boundary. This suggests that the upstream flow redistribution is responsible for enabling the fan to operate stably within such a severe inlet distortion.

Five points for orbit LE are marked as *a*, *b*, *c*, *d*, and *e* on Figs. 12 and 13. These are included to identify the key locations around the annulus in terms of strong fan-distortion interaction and steep gradients in the flow field. At point *a* the rotor is moving from the distorted sector towards the clean one. At this position, the mass flow is low and the induced swirl creates positive incidence onto the blades leading to high pressure ratio (higher effective rotational speed). Point *b* is an intermediate point used in the discussion below. Point *c* is just within the clean sector (higher mass flow) but positive incidence is still significant; hence the mass flow and pressure ratio are both high. From this point, the positive incidence reduces in the direction of the rotor rotation and it crosses zero at a local operating point that coincides with the steady characteristic. The incidence becomes then negative (lower effective rotational speed), which decreases further the total pressure ratio until it reaches a minimum at point *d*. The rotor then moves back into the distorted sector. At point *e*, a minimum in mass flow is reached, as the incidence is still negative and the rotor is back in the distorted sector. From there on, as the rotor continues clockwise through the distorted sector, the incidence starts increasing again, raising the pressure ratio back towards point *a*.

In summary, the local operating point of the rotor can be understood by considering the variations in swirl angle and mass flow rate present upstream of the rotor.

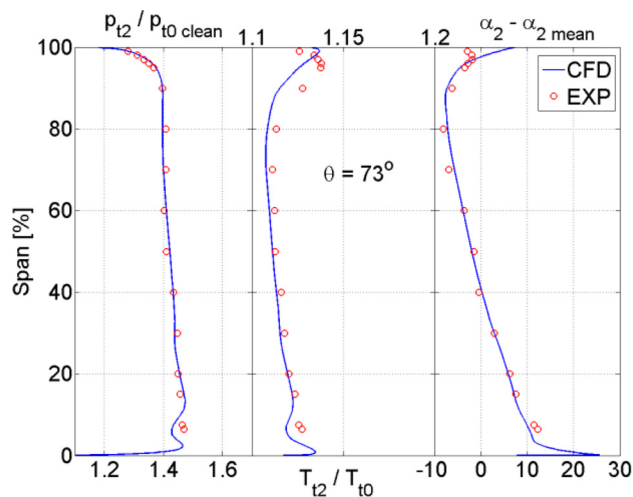


Fig. 19 Time-averaged radial traverses downstream of the rotor at circumferential position $\theta = 73$ deg

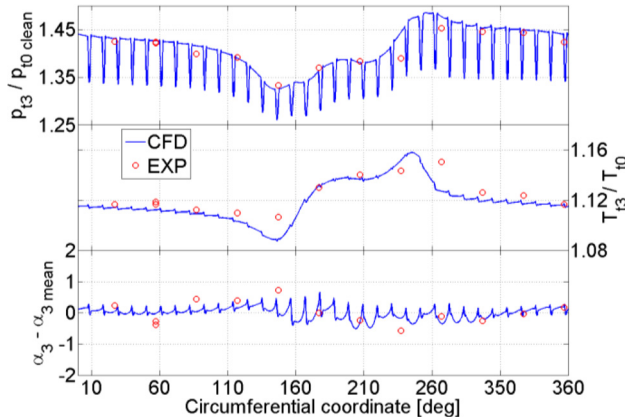


Fig. 20 Time-averaged circumferential traverses downstream of the OGV at midspan

Observed Distortion Transfer

Figure 14 shows absolute-frame, time-averaged stagnation pressure and temperature contours downstream of the rotor. From the latter, it is easy to identify the regions with highest and lowest work input (highest/lowest Δh_t). The regions of lowest and highest work input are not so evident in the stagnation pressure plot. The issue of the existence of an angular shift between the maxima (or minima) of total pressure and temperature downstream of a rotor facing distorted flow conditions has been raised in previous papers [24,25]. The results shown here indicate that the main driver for this difference is simply the fact that flow particles receiving the highest amount of work input may have originated within a region of low total pressure at inlet.

We will focus on the discussion of the present test case to illustrate this idea. As mentioned already, work input mainly depends on two things: inlet mass flow (axial velocity) and incidence (swirl – tangential velocity). If we go back now to the sectors defined in the previous section (Fig. 12, bottom), we can visually match inlet and exit regions in Figs. 14 and 15 to aid the understanding. In Fig. 14 (right) the region with highest stagnation temperature increase at exit (highest work input) lies between sectors *a* and *b*. If we then look at the same sectors at inlet, it can be seen (using Fig. 15) that they sit in a region of high counter-swirl and low/medium axial velocity. More precisely, the region in between is likely to present a combination of these two factors for which the work input peaks. This is consistent with Fig. 13 showing sector *a* (closely followed by sector *b*) being the point with the highest total pressure *ratio*. In terms of absolute exit stagnation pressure, it is clear from Fig. 14 (left) that its value for sector *b* is larger. This makes sense when one realizes that the inlet stagnation pressure of sector *b* was higher at inlet. Similar arguments can be applied to relate the region with minimum work input to the sector with lowest total pressure *ratio* and to that with lowest exit total pressure. Note also that the angular shift of exit stagnation quantities observed in this test case is small relative to those seen in previous papers. The reason for that can be attributed to the fact that the variations in inlet p_t of this particular distortion pattern occur over very small angular extensions and that the test case is a single stage. Thus, there is limited space for the appearance of such shifts.

Figure 16 shows radial and circumferential particle displacement between the rotor LE and TE, which is an indication of flow redistribution through the rotor passages. These displacements are obtained from the absolute-frame time-averaged solution already mentioned. In general, the distorted sector presents higher circumferential displacements associated to a higher residence time (lower velocities across the passage). It can also be seen some vertical fluid motion in the region where the “jet” formed ahead of the rotor LE is coming out of the passage. The existence of a strong circumferential redistribution of mass occurring within the

rotor passage associated to that region is also clear (see dashed lines). The average level of radial displacement across the distorted sector is greater as well. In addition, the presence of steep gradients from the upstream flow as well as the three dimensionality of the flow close to the hub is clear.

Note that the jet formed ahead of the stage, close to the hub region, persists downstream of the rotor as Fig. 17 (right) reveals in the form of a localized region with unusually high radial velocity. Figure 17 (left) also shows contours of mass flux at exit, which indicate how mass-flux variations and upstream swirl not only modify the work input but also the rotor’s local capacity.

Figure 18 shows a comparison between numerical and experimental circumferential traverses of stagnation pressure and temperature as well as absolute whirl angle at midspan at measurement

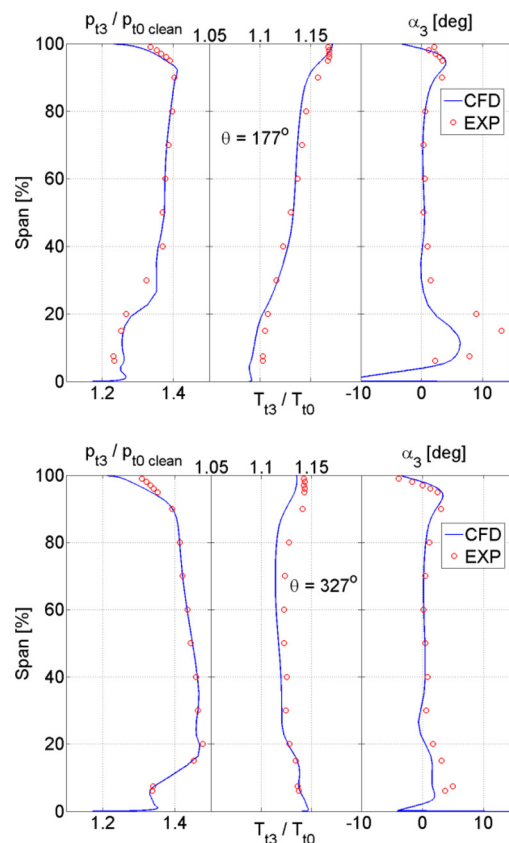


Fig. 21 Time-averaged radial traverses downstream of the OGV for $\theta = 177$ deg (top) and $\theta = 327$ deg (bottom)

station 2 (downstream of the rotor). As it can be seen, predicted transfer of the distortion downstream is consistent with the experimental results. The only slight mismatch occurs near the region where the rotor leaves the distorted sector: total pressure is overestimated and total temperature is underestimated respectively in two consecutive regions.

Additionally, Fig. 19 shows a comparison between numerical and experimental radial traverses of the same quantities at a given circumferential position downstream of the rotor.

Figure 20 shows a comparison between experimental and numerical circumferential traverses at midspan downstream of the OGV. As for the rotor, the agreement is good. Additionally, two radial traverses are shown: Fig. 21 (top) corresponds to a circumferential position within the distorted region, while Fig. 21 (bottom) corresponds to a position within the clean sector. The agreement is good, apart from the absolute value of flow angle in the hub region, dominated by the OGV secondary flows and hub separations in the rotor.

To complete the flow description, Fig. 22 shows unwrapped blade-to-blade snapshots of stagnation pressure and temperature as well as static pressure at 90% span. The black dotted lines indicate the boundaries of the distorted sector at inlet. The top picture shows how the stagnation pressure pattern is convected axially through the duct until it reaches the fan face. The fluid that the rotor works hardest on can be easily tracked by following the regions of high total temperature at rotor exit. The flow with highest total temperature originates in the distorted sector, where the incoming mass flux is low, close to the boundary with the clean

flow sector, where the counter-swirl is high. Conversely, the region of flow with the lowest total temperature originates in the clean sector, where there is high mass flux and high co-swirl. This is consistent with the findings from the study of the operating point variations. The variation in work input combined with the inlet total pressure pattern determines the total pressure distortion that is transferred downstream. As illustrated in Fig. 22, and as discussed above, there is little phase shift between the downstream variations in stagnation pressure and temperature.

The bottom picture in Fig. 22 shows how the variation in shock structure in the rotor passages and the associated static pressure ahead of the rotor are affected by the variation in local operating condition. In the clean sector, the passage shock is well swallowed with an additional bow shock standing forward of the LE. As the rotor moves into the distorted sector, the passage shock gradually gets stronger and moves forward due to a higher relative flow acceleration in the front suction surface. Eventually the passage and bow shocks merge into a single normal shockwave that stands expelled.

The shock structure also influences the static pressure field downstream of the rotor, which is also nonuniform. As a result, the OGV must deal with a highly distorted inlet flow. The stagnation pressure distortion is attenuated by the rotor, but stagnation temperature, static pressure, and absolute flow angle distortions are generated. Flow angles will have an impact on the OGV loading, while stagnation temperature will modify its local mass-flow capacity. Stagnation quantities convect through the OGV, while static pressure and whirl angle asymmetries are greatly suppressed. In the top picture of Fig. 22, a circumferential variation

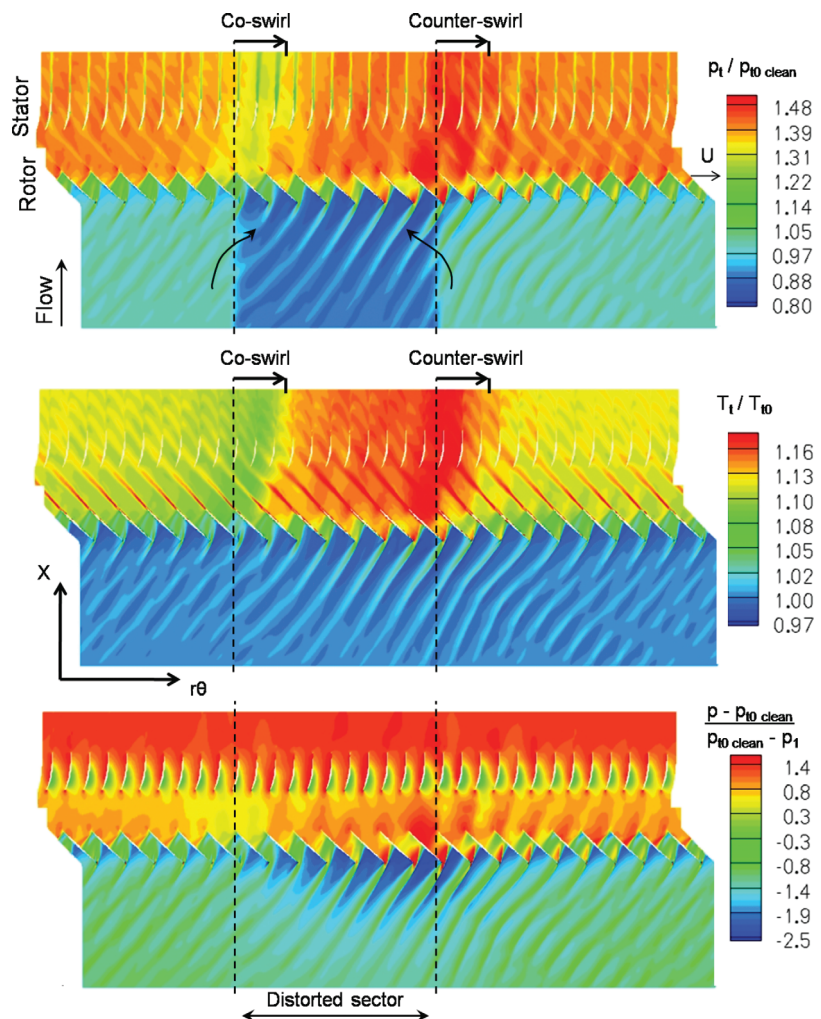


Fig. 22 Unwrapped blade-to-blade snapshots at 90% span of stagnation pressure and temperature and static pressure

in the thickness of the OGV wakes is visible, illustrating the extent of the variation of the OGV local operating condition.

Conclusions

The aerodynamics of NASA rotor 67 transonic fan-stage operating with a 120 deg stagnation pressure circumferential distortion have been investigated by means of high-fidelity, full-annulus, unsteady CFD. Previously unpublished experimental data have been used to validate the numerical results and the agreement is found to be good, demonstrating the suitability of the solver for this application.

The redistribution of the approaching flow upstream of the stage is shown to be the mechanism that enables the rotor to accommodate a high level of circumferential inlet distortion. The associated induced swirl is shown to greatly affect work input and the fan rotor local operating conditions. An absolute-frame, time-averaged solution is obtained for the rotor domain and used to divide the flow up into sectors to calculate consistently the locus of the rotor local operating point on the performance map. This variation in operating conditions is shown to be mainly determined by the inlet swirl and mass flow distributions at the fan leading edge (inlet velocity triangles).

The attenuation of the stagnation pressure distortion as well as the generation of stagnation temperature, static pressure, and absolute whirl angle distortions downstream of the rotor are understood in terms of the inlet conditions and the variation of work input from the rotor. These effects also cause a variation in the rotor shock wave structure and determine any phase shift between the downstream stagnation quantities.

Acknowledgment

The authors would like to thank Rolls-Royce plc and EPSRC for funding this work and for the permission to publish this paper. Anthony Strazisar and Sue Prahst at NASA Glenn Research Center are gratefully acknowledged for providing the experimental data and support. At the Whittle Laboratory, special thanks to Tom Hynes and Hao Xia for the insightful advice and for the support in the development of post-processing tools; John Longley and Liping Xu are also acknowledged for their comments on this paper. At Rolls-Royce plc, Tony Rae, Donald Madden, and Paul Field, from Compressors, are acknowledged for their constructive comments and ideas; Leigh Lapworth and Andrea Milli, from Aerothermal Methods, are thanked as well for their support with the solver and grid generator. Stuart Rankin and the University's High Performance Computing Service are also thanked for their support and for making the Darwin cluster available to the project.

Nomenclature

AR	= aspect ratio
C_{ax}	= blade axial chord
D	= fan diameter
DC_{120}	= distortion parameter based on a 120 deg sector
FPR	= fan pressure ratio
h	= enthalpy
LE	= leading edge
M	= Mach number
N	= shaft speed (rpm)
OGV	= outlet guide vane
p	= pressure
r_h/r_t	= hub-to-tip radii ratio
St.	= station
T	= temperature
TE	= trailing edge
u	= velocity component
U	= blade speed
X	= axial coordinate
α	= absolute whirl flow angle

β = relative whirl flow angle

Δ = increment

ζ = radial flow angle

η = efficiency

θ = circumferential coordinate

ρ = density

Φ = flow coefficient

ψ = loading coefficient

Subscripts

clean = nondistorted sector value

is = isentropic

LE = value at leading edge station

rel = relative frame quantity

t = stagnation quantity

x = axial component

0, 1, 2 and 3 = measurement stations

θ = circumferential component

∞ = free-stream

References

- [1] Ehrich, F., 1957, "Circumferential Inlet Distortions in Axial Flow Turbomachinery," *J. Aero. Sci.*, **1**, pp. 413–417.
- [2] Seidel, B. S., 1964, "Asymmetric Inlet Flow in Axial Turbomachines," *ASME J. Eng. Power*, **1**, pp. 18–28.
- [3] Doyle, M. D. C., and Horlock, J. H., 1966, "Circumferential Asymmetry in Axial Flow Compressors," *J. R. Aero. Soc.*, **70**, pp. 956–957.
- [4] Plourde, G. A., and Stenning, A. H., 1968, "Attenuation of Circumferential Inlet Distortion in Multistage Axial Compressors," *J. Aircraft*, **5-3**, pp. 238–242.
- [5] Callahan, G. M., and Stenning, A. H., 1971, "Attenuation of Inlet Flow Distortion Upstream of Axial Flow Compressors," *J. Aircraft*, **8-4**, pp. 227–233.
- [6] Henderson, R. E., and Horlock, J. H., 1972, "An Approximate Analysis of the Unsteady Lift on Airfoils in Cascade," *ASME J. Eng. Power*, **1**, pp. 233–240.
- [7] Greitzer, E. M., 1973, "Upstream Attenuation and Quasi-Steady Rotor Lift Fluctuations in Asymmetric Flows in Axial Flow Compressors," *ASME Paper 73-GT-30*.
- [8] Horlock, J. H., Greitzer, E. M., and Henderson, R. E., 1977, "The Response of Turbomachinery Blades to Low Frequency Inlet Distortions," *ASME J. Eng. Power*, **1**, pp. 195–203.
- [9] Greitzer, E. M., and Strand, T., 1978, "Asymmetric Swirling Flows in Turbomachinery Annuli," *ASME J. Eng. Power*, **100**, pp. 618–629.
- [10] Stenning, A. H., 1980, "Inlet Distortion Effects in Axial Compressors," *ASME J. Fluids Eng.*, **102**, pp. 7–13.
- [11] Hynes, T. P., and Greitzer, E. M., 1987, "A Method for Assessing Effects of Circumferential Flow Distortion on Compressor Stability," *ASME J. Turbomach.*, **109**, pp. 371–379.
- [12] Moore, F. K., 1984, "A Theory of Rotating Stall of Multistage Compressors, Parts I–III," *ASME J. Eng. Gas Turbines Power*, **106**, pp. 313–336.
- [13] Greitzer, E. M., Mazzawy, R. S., and Fulkerson, D. A., 1978, "Flow Field Coupling Between Compression System Components in Asymmetric Flow," *ASME J. Eng. Power*, **100**, pp. 66–72.
- [14] Mazzawy, R. S., 1977, "Multiple Segment Parallel Compressor Model for Circumferential Flow Distortion," *ASME J. Eng. Power*, **99**, pp. 288–296.
- [15] Longley, J. P., and Greitzer, E. M., "Inlet Distortion Effects in Aircraft Propulsion System Integration," AGARD Lecture Series, **1**.
- [16] Dunham, J., 1965, "Non-Axisymmetric Flows in Axial Flow Compressors," *Mech. Eng. Sci. Mono.*, **3**, pp. 1–32.
- [17] Hawthorne, W. R., Mitchell, N. A., and McCune, J. E., 1978, "Non-Axisymmetric Flow Through Annular Actuator Disks: Inlet Distortion Problem," *ASME J. Eng. Power*, **100**, pp. 604–617.
- [18] Horlock, J. H., 1978, *Actuator Disk Theory. Discontinuities in Thermo-Fluid Dynamics*, McGraw-Hill, New York.
- [19] Hsiao, E., Naimi, M., Lewis, J. P., Dalbey, K., Gong, Y., and Tan, B., 2001, "Actuator-Duct Model of Turbomachinery Components for Powered-Nacelle Vavier-Stokes Calculations," *ASME J. Propulsion Power*, **17-4**, pp. 919–927.
- [20] Xu, L., 2002, "Assessing Viscous Body Forces for Unsteady Calculations," *ASME Paper GT2002-30359*.
- [21] Hah, C., Rabe, D. C., Sullivan, T. J., and Wadia, A. R., 1998, "Effects of Inlet Distortion on the Flow Field in a Transonic Compressor Rotor," *ASME J. Turbomach.*, **120**, pp. 233–246.
- [22] Yao, J., Gorrell, S. E., and Wadia, A. R., 2007, "A Time-Accurate CFD Analysis of Inlet Distortion Induced Swirl in Multistage Fans," *AIAA Paper 2007-5059*.
- [23] Gorrell, S. E., Yao, J., and Wadia, A. R., 2008, "High Fidelity URANS Analysis of Swirl Generation and Fan Response to Inlet Distortion," *AIAA Paper 2008-4985*.
- [24] Yao, J., Gorrell, S. E., and Wadia, A. R., 2008, "High-Fidelity Numerical Analysis of Per-Rev-Type Inlet Distortion Transfer in Multistage Fans—Part I: Simulations With Selected Blade Rows," *ASME Paper GT2008-50812*.
- [25] Yao, J., Gorrell, S. E., and Wadia, A. R., 2008, "High-Fidelity Numerical Analysis of Per-Rev-Type Inlet Distortion Transfer in Multistage Fans—Part II: Simulations With Selected Blade Rows," *ASME Paper GT2008-50813*.

- II: Entire Component Simulation and Investigation," ASME Paper GT2008-50813.
- [26] Strazisar, A. J., Wood, J. R., Hathaway, M. D., and Suder, K. L., 1989, "Laser Anemometer Measurements in a Transonic, Axial-Flow, Fan Rotor," NASA Technical Paper 2879.
- [27] Cunnan, W. S., Stevans, W., and Urasek, D. C., 1978, "Design and Performance of a 427-Meter-Per-Second-Tip-Speed Two-Stage Fan Having a 2.40 Pressure Ratio," NASA Technical Paper 1314.
- [28] Urasek, D. C., Gorrel, W. T., and Cunnan, W. S., 1979, "Performance of Two-Stage Fan Having Low-Aspect-Ratio, First-Stage Rotor Blading," NASA Technical Paper 1493.
- [29] Hathaway, M. D., 1986, "Unsteady Flows in a Single-Stage Transonic Axial-Flow Fan Stator Row," NASA Technical Memorandum 88929.
- [30] Suder, K. L., Hathaway, M. D., Okiishi, T. H., Strazisar, A. J., and Adamczyk, J. J., 1987, "Measurements of the Unsteady Flow Field Within the Stator Row of a Transonic Axial-Flow Fan. I—Measurement And Analysis Technique," NASA Technical Memorandum 88945.
- [31] Hathaway, M. D., Suder, K. L., Okiishi, T. H., Strazisar, A. J., and Adamczyk, J. J., 1987, "Measurements of the Unsteady Flow Field Within the Stator Row of a Transonic Axial-Flow Fan. II—Results And Discussion," NASA Technical Memorandum 88946.
- [32] <http://www.grc.nasa.gov/WWW/5810/w8.htm>.
- [33] Lapworth, B. L., 2004, "HYDRA-CFD: A Framework for Collaborative CFD Development," International Conference on Scientific and Engineering Computation IC-SEC.
- [34] Spalart, P. R., and Allmaras, S. R., 1994, "A One-Equation Turbulence Model for Aerodynamic Flows," *Rech. Aero.*, **1**, pp. 5–21.
- [35] Vahdati, M., Sayma, A. I., Freeman, C., and Imregun, M., 2005, "On the Use of Atmospheric Boundary Conditions for Axial-Flow Compressors Stall Simulations," *ASME J. Turbomach.*, **127**, pp. 349–351.
- [36] Shahpar, S., and Lapworth, B. L., 2003, "PADRAM: Parametric Design and Rapid Meshing System for Turbomachinery Optimisation," ASME Paper GT2003-38698.
- [37] Adamczyk, J. D., 1985, "Model Equation for Simulating Flows in Multistage Turbomachinery," ASME Paper 85-GT-226.